INTERNATIONAL ATOMIC ENERGY AGENCY
UNITED NATIONS EDUCATIONAL, SCIENTIFIC AND CULTURAL ORGANIZATION

INTERNATIONAL CENTRE FOR THEORETICAL PHYSICS
34100 TRIESTE (ITALY) - P.O.B. 586 - MIRAMARE - STRADA COSTIERA 11 - TELEPHONES: 224281/2/3/4/5/6
CABLE: CENTRATOM - TELEX 460392 - 1

H4.SMR/164 - 23

WORKSHOP ON CLOUD PHYSICS AND CLIMATE

23 November - 20 December 1985

CLOUD PRECIPITAION PROCESSES

Part VII

DEEP STRATIFORM CLOUDS AND OROGRAPHIC INFLUENCES

G. VALI
University of Wyoming
U.S.A.

LECTURE 7 - DEEP STRATIFORM CLOUDS

Selected references:

Overall organization described in references listed for mid-latitude applications.

Browning and Harrold 1969, QJRMS pp 288-309
Herzegh and Hobbs 1980, J. Atm. Sci. pp 597-
Heymsfield 1977 J. Atm. Sci. p367
Lo + Passarelli, 1982 J. Atm. Sci. p697
Borovikov + Nevzorov, 1971 in 'Cloud Physics' by Borovikov
Carbone + Bohne, 1975 J. Atm. Sci. p1384
Lin, Farley and Orville, 1983, J. Climate Appl. Meteor. 1065
Orville et al 1984, J. Climate Appl. Meteor p1585-1600
Atkinson and Smithson 1978, Mt. Wea. Rev., p211-222
Sanders and Bosart 1985 J. Atm. Sci. p 1398-1407

Mesoscale characteristics dominate, not cloud-scale (~10 km), hence more difficult to describe, and to observe

Major producers of precipitation, low to moderate intensity.

Typically composed of ice (at mid-latitudes), except for small patches of LWC. Origin of ice suspected at upper levels, growth by diffusion and aggregation.

Some upper-level instability may be present and lead to "generating cells"; these produce local increases in precipitation.

Role of melting layer.

OROGRAPHIC INFLUENCES

Some references:

Bergeron 1960 in Geophys. Monogr. #5

Pomerelli and Bochume, 1983 M. Wea. Rev. p 1062

Gocho 1978 J. Met. Soc. Japan p 405

Browning et al 1974, QJRMS p ~~320~~ 309

Carruthers + Choularton, 1983, QJRMS p 578

Cotton 1982 J. Rech. Atm. p 310

Hanuity 1983 J. Atm. Sci. p 1218

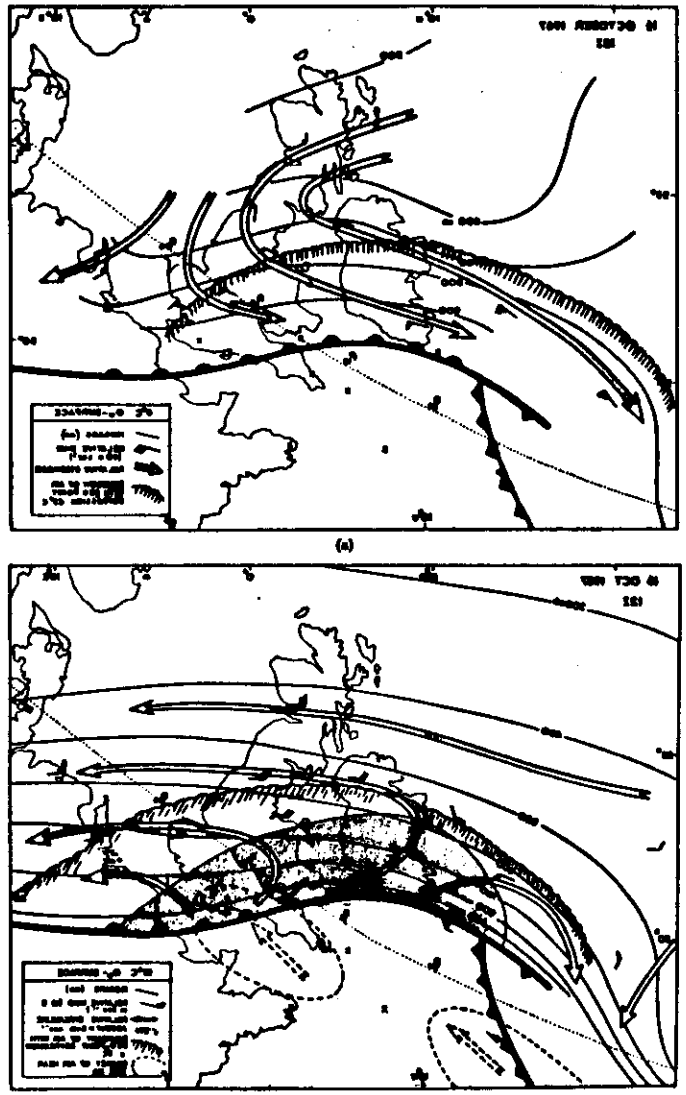

θ_w-analyses have been carried out [illegible] data from routine radiosonde ascents released at 1130 [illegible] Pershore at 1046, 1124, 1212 and 1314 Z and further [illegible] placed according to the system velocity. Contour pre[illegible]senting θ_w-surfaces at 1°C intervals from 6° to 16°C. [illegible] θ_w of 6° and 12°C, respectively, are reproduced in Fig. 2 (a) and (c). [illegible] surfaces was situated near the base of the frontal zone; the second was situated near the top of the frontal zone. A complicating factor in the analysis was that pockets of air with a θ_w of 12°C and less were embedded within air having a generally rather higher θ_w in the warm sector. These pockets were centred near the 700-mb level and their 'coldest' parts are depicted in Fig. 2 (b) by the dashed contours.

The solid arrows in Fig. 2 (a) and (b) represent streamlines in the 6° and 12° θ_w-surfaces *relative to the system*. Over Britain descent predominated in the 6°C surface at the base of the warm frontal zone and ascent predominated in the 12°C surface at the top of this zone. Large-scale ascent in excess of 5 cm s^{-1} occurred over an extensive area (stippled in Fig. 2 (b)). The size of this area was broadly matched by the extent of frontal rain at the surface. Over Pershore the vertical velocities in the 6° and 12° θ_w-surfaces at 12 Z are estimated to have been -5 ± 2 and $+16 \pm 8$ cm s^{-1} respectively. Corresponding vertical velocities estimated from the other surfaces are listed in Table 1. The probable errors in w in the third column arise from uncertainties in the orientation of the θ_w surfaces; for a given uncertainty in this orientation the error in w is proportional to the magnitude of the relative wind. Also shown for comparison in Table 1 are the mean vertical velocities between 1130 and 1230 Z obtained from the Doppler radar data in Part II of this paper. Agreement is good, with both sets of data showing weak descent at low levels changing to ascent within and above the warm frontal zone.

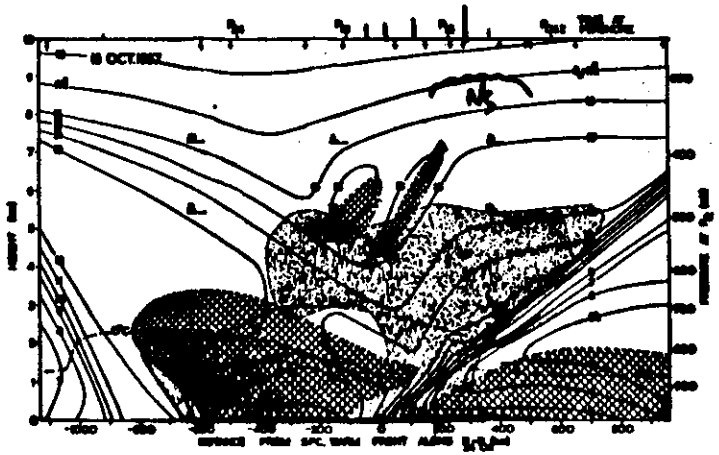

Figure 2. Analysis for vertical section along 245° through Pershore at 12 Z 16 October 1967. Solid lines are lines of constant θ_w. Wind barbs represent the component of the wind in the section relative to the system, a full barb being 5 m s^{-1}. Cross-hatching denotes potential instability. Stippling denotes moist air with dew point depression ≤ 3°C. The heavy line along the distance scale represents the overall extent of continuous and intermittent rain at the surface, ending at the passage of the surface cold front. The scale P_W–P_m at the top of the diagram represents time at Pershore assuming a translation velocity of 16 m s^{-1}. The arrows along the top of the diagram indicate the locations of radiosonde ascents.

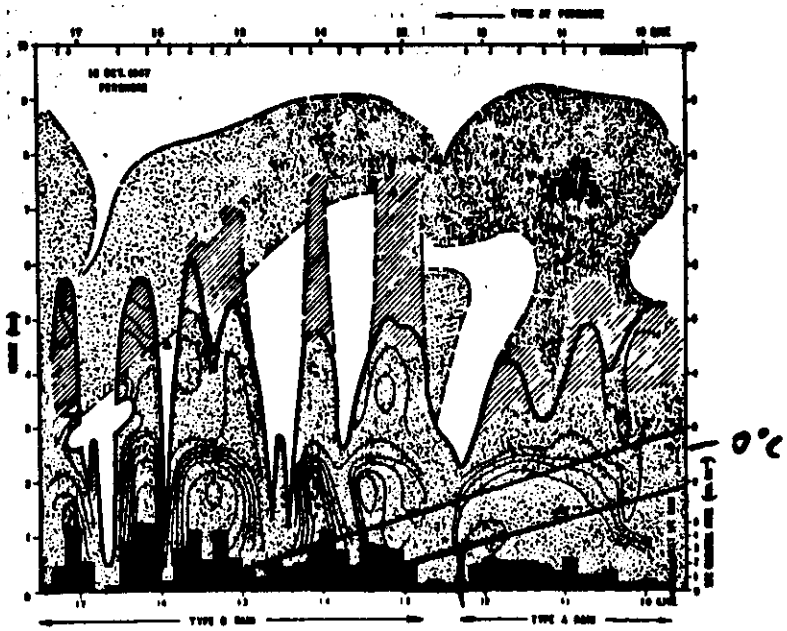

Figure 12. Time-height section showing the vertical distribution of precipitation echo in the vicinity of the warm front at Pershore. The warm frontal zone is indicated by the two straight lines. The heavy solid contours represent the extent of echo detected by the Doppler radar at Pershore when its aerial was pointing vertically. The thin solid isopleths at intervals of 1 m s^{-1} represent the reflectivity-weighted mean particle fallspeed V_f measured by the Doppler radar. The melting level is situated where V_f changes sharply in the vertical from 2 to 3 m s^{-1}. The heavy dashed contours represent the extent of relatively weak echo detected at higher levels by the TPS-10 radar. Areas where clusters of precipitation generators were observed are shown hatched. Surface rainfall rate at Pershore is plotted at the bottom of the diagram.

positively with the surface rainfall rate (plotted along the abscissa). During the period of Type *A* rain, however, from 0930 to 1230 Z, the correlation was inverse. According to Harrold and Nicholls (1968) this is a common occurrence in warm frontal rain. It is partly a result of evaporation beneath the frontal zone within the relatively dry subsiding air at the leading edge of the rain area; nearer the position of the surface warm front the same low-level air has become much moister due to its previous passage through the rain area.

The vertical extent of echo detected by the TPS-10 radar (dashed contours in Fig. 12) was greater than that detected by the Doppler radar. Not only was it able to detect the upper parts of the generator cells (Fig. 11 (d)) but it also detected an extensive layer of weak echo some 2 to 3 km thick which was centred at about 8 km until 13 Z and subsequently lowered. The Type B_1 rain areas which passed over Pershore after 13 Z were associated with mesoscale clusters of high level generator cells; although individual generators were only a few km across (Fig. 11 (d)) the meso-scale clusters (indicated by diagonal hatching in Fig. 12) were typically 50 km across. The generators themselves

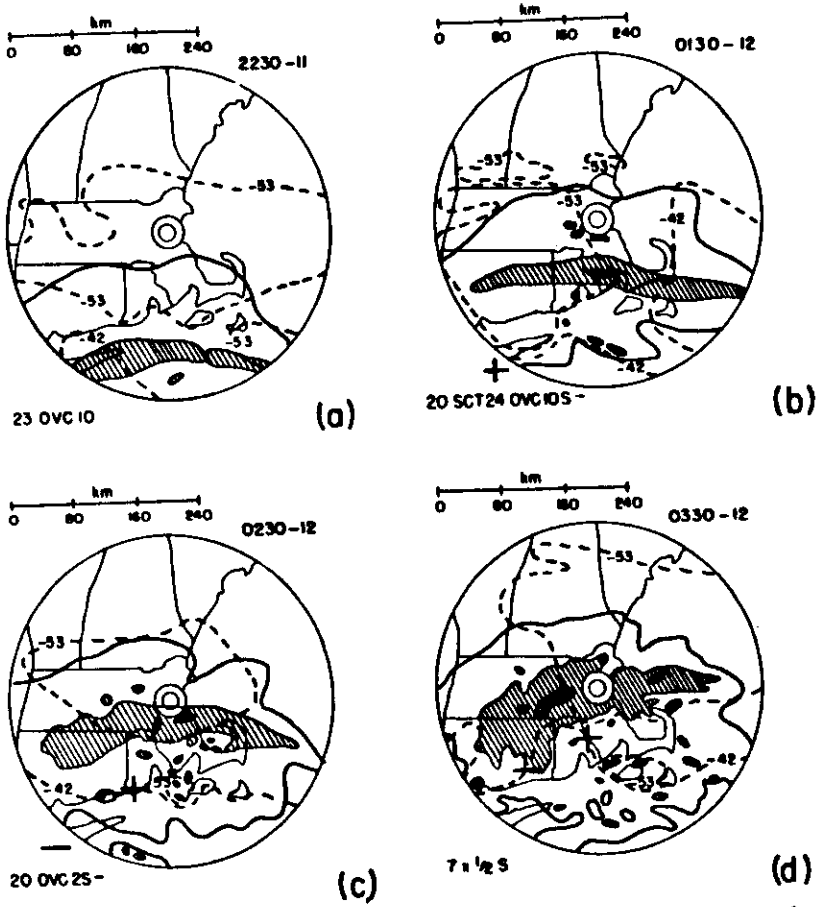

FIG. 1. Smoothed CAPPI maps for MIT radar at selected times (GMT) and dates (February) as indicated, for the layer from 2.5 to 4 km. Solid contours are for 15 dBZ, 25 dBZ (shaded), and 30 dBZ (cross-hatched). Dashed lines are cloud top isotherms, estimated from GOES infrared imagery, for 30 min after time of CAPPI map. Plus and minus signs show position of maximum rise and fall of surface pressure associated with the large-amplitude gravity wave. Heavy line on (b) (0730 GMT map) indicates position of RHI cross section shown in Fig. 2. Conventional surface observations at Boston, MA (BOS) 30 min after times of CAPPIs are added. Numerals I, II, and III in (b) and (c) denote persistent multiple bands.

strengthened and became reconsolidated at 0530 GMT (Fig. 1f) as the mesoscale depression moved eastward and dissipated. The heaviest snow was reported at BOS during this passage of the gravity wave, as at many other stations to the southwest (BS). Further complications arose immediately as the line, together with the thermal wind, began to rotate counterclockwise in response to the passage of the synoptic-scale cyclone. This development was accompanied by bifurcation of the line, as though it contained two centers of rotation, one east and one west of MIT. The development was partly obscured by a radar shadow extending northeastward from the transmitter, but the two lines (I and II) were clearly separated by

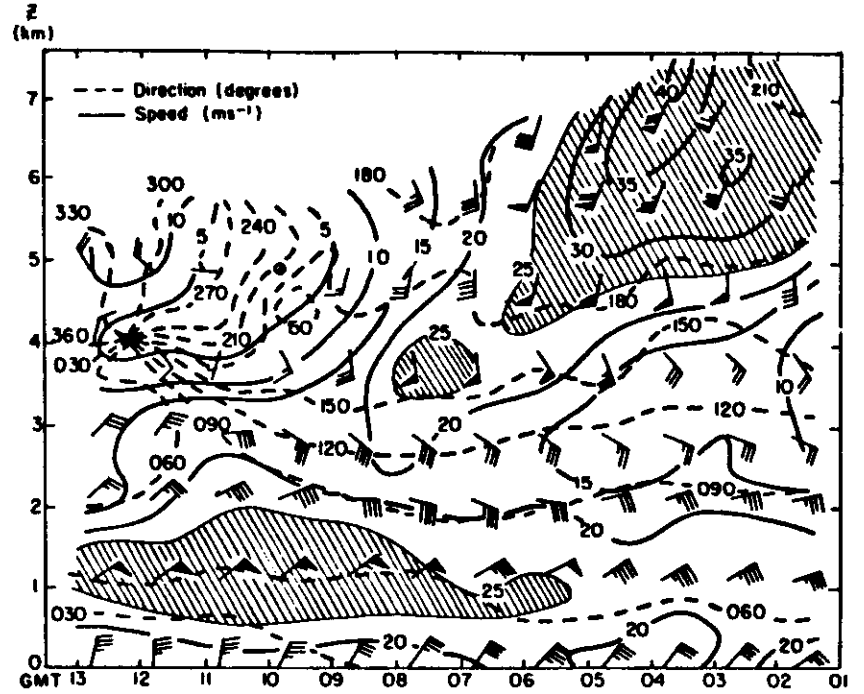

FIG. 3. VAD time-height sections from MIT radar 12 February: (a) direction (dashed isogons at intervals of 30 degrees) and speed (solid isotachs at intervals of 5 m s^{-1}); (b) vertical motion ω at intervals of 10×10^{-3} mb s^{-1}. Heavy dashed lines are levels of nondivergence. Columns of numbers at right are standard deviation of divergence, in units of 10^{-5} s^{-1}; (c) condensation rate, in units of 10^{-6} g cm^{-3} s^{-1} for 50 mb layers. Column totals (in mm of liquid water h^{-1}) are shown along abscissa, denoted by Σ and accompanied by intensity of snow observed at Boston, MA (BOS).

these oscillations clearer. The u "jet" was descending from $x = 65$ to 25 km where reflectivity was relatively feeble. Weak ascent is seen at $x = 15$ just upwind from the weakening and southeast of MIT. Sharp descent of 40×10^{-3} mb s^{-1} ($w = -55$ cm s^{-1}) occurred more or less over MIT culminating in a zone of minimum reflectivity at $x = -10$ km, where band separation was occurring. Then, strong ascent with peak $\omega = -90 \times 10^{-3}$ mb s^{-1} ($w = 110$ cm s^{-1}) was seen at $x = -25$ km, upstream from the largest reflectivities in the section, in the vigorous band between $x = -30$ and -55 km. (The general descent beyond $x = -65$ km may have been overstated, since it is mainly the result of strong apparent divergence at the lowest levels. This is probably a spurious consequence of beam broadening and loss of shallow positive u components below the radar horizon at this range. Surface observations in and beyond this region showed northerly wind components.) Finally, maxima of ascent at the top of the Doppler data near $x = 35$ km and $x = -15$ km appear to be separate perturbations on another barely detectable streak of maximum negative u components at and above the 450 mb level. The prominent minima of radial component magnitude near 500 mb, and near 750 mb between $x = -25$ km and -40 km are further evidence of vertical layering.

Both this layering and the longitudinal oscillations in the cross-front circulation (associated with the band breakup in Fig. 1) indicate structure not explainable in terms of a single zone of frontogenetical forcing. Hoskins *et al.* (1984) have demonstrated the theoretical possibility of multiple frontal structure if large-scale frontogenesis operates on an initially irregular temperature field, but the multiple character is apparently shallow, contrary to our observations. Seltzer *et al.* (1985) have recently shown evidence for symmetric instability, in this case in the layer 2.5–

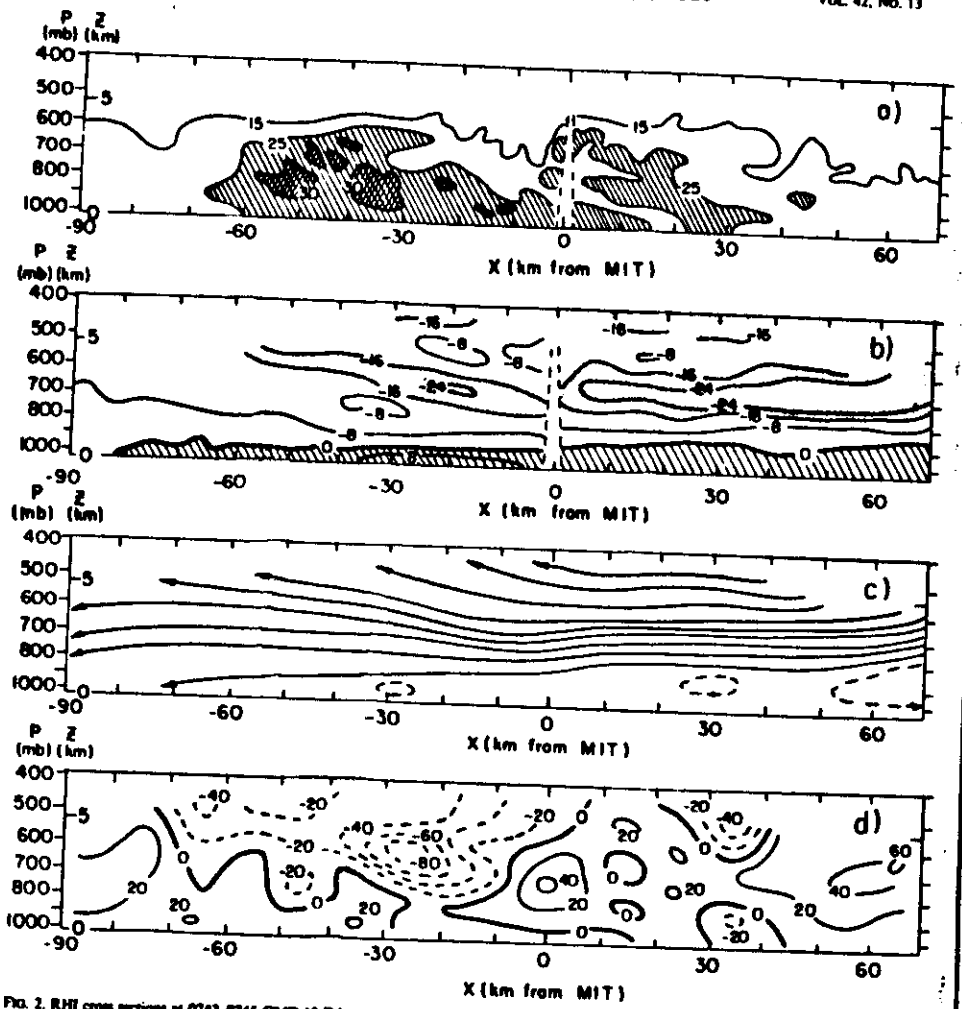

Fig. 2. RHI cross sections at 0743–0745 GMT 12 February: (a) radar reflectivity (dBZ); (b) radial component of wind, with isotachs at intervals of 8 m s^{-1}; (c) ψ' (at intervals of 8×10^3 mb m s^{-1}); (d) ω' (at intervals of 20×10^{-3} mb s^{-1}).

16 m s^{-1}) at its limit of detectability (near $x = -60$ km). It clearly resembles the ageostrophic wind-signature response to synoptic-scale frontogenetical forcing, seen in SB. The center of the ribbon approximately separated descending streamlines below from ascending ones above (as seen in Fig. 2c). The horizontally averaged vertical motions were modest, ranging from 13×10^{-3} mb s^{-1} at 750 mb ($w = -13$ cm s^{-1}) to -14×10^{-3} mb s^{-1} at 450 mb ($w = 24$ cm s^{-1}).

Prominent oscillations with wavelengths of the order of 30–60 km can be seen along the high speed ribbon in Fig. 2c. The vertical motions obtained by differencing ψ' over 10 km distances (Fig. 2d) make

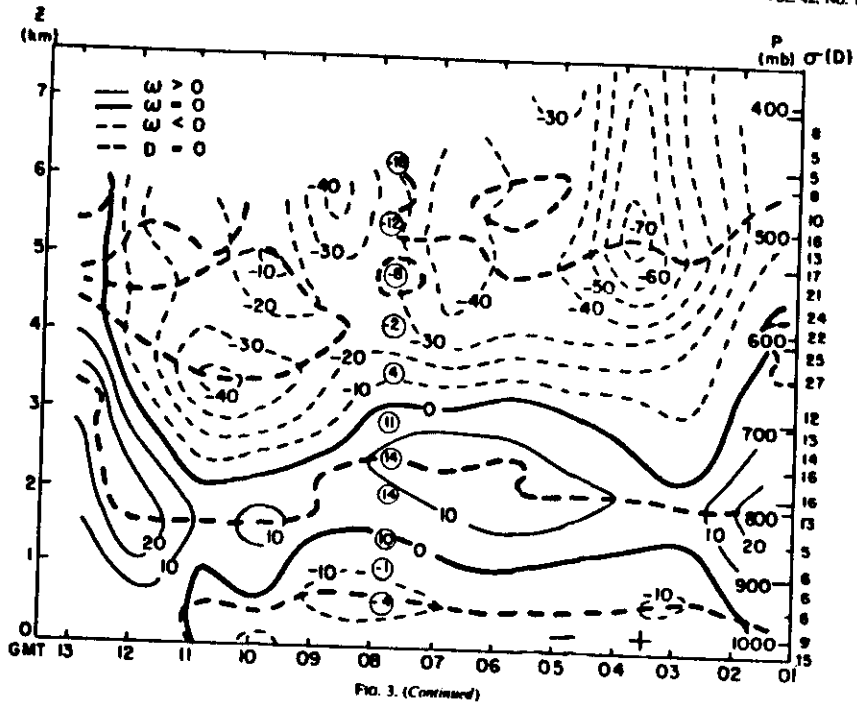

Fig. 3. (*Continued*)

5.25 km, but on the basis of the shear of the observed wind. Sanders and Bosart showed that this shear was highly ageostrophic, but that instability was present in about the same layer on a geostrophic basis. Seltzer *et al.* (1985) examined this case at a time when only a single precipitation band was visible on radar, but found in other cases an expected spacing between bands ranging from about 50 km to about 150 km. The observed layering implies a horizontal spacing near or above the upper limit of this range, while the oscillations and the multiple bandedness show spacing near the short end of the range and extend near or below the lower extremity of the unstable layer. Thus, while symmetric instability provides a plausible explanation of these irregularities, we cannot rule out other candidates.

4. Velocity azimuth displays (VADs)

The time history of the motion field and its implications for precipitation were obtained from a series of hourly VAD (Browning and Wexler, 1968) calculations through the duration of the storm, from 0145 to 1245 GMT. These refer to a vertical cylindrical volume with nominal radius 20 km centered at MIT, with data taken at vertical intervals of approximately 300 m. (To provide this vertical resolution up to 6.8 km with the limited available number of scanning elevation angles up to 15 degrees, it was necessary to use radii ranging from 14–26 km.) A vertical time section of area-averaged wind direction and speed is shown in Fig. 3a. Some subjective judgment was used at both the base and the top of the display. At the bottom, points in the northeast sector were found to represent return from high waves in Massachusetts Bay (visible because of the high altitude of the radar, not an alarming sea state) and were ignored. The upper limit was taken as the highest elevation at which data points were available in more than half of the 30° sectors comprising the circle. The assumed quasi-sinusoidal variation of radial wind component with azimuth was used as a guide in analysis of these marginal circles, where the uncertainty is relatively large. In Fig. 3a we see that northeasterly winds occurred throughout the storm at and below 1 km, becoming generally stronger with time. In all but the latest part, the wind veered with elevation, reaching south or south-southwest around 5 km. Maximum speed in this southerly current descended and weak-

ample, the
ter of Fig.
n Fig. 1b,
: 1040 PST
seemed to
which was
al surface.
during the
2, Fig. 2a)
more con-
s and slop-
ted by the
evaporated
e slopes of
, which are
atal winds,
associated
bout 5 km,
with height
ly vertical,
ed with the
is region.
ility and in-
with cloud
. the tops of
t the trails,
riginated in
. The orien-
suggest that
linear arrays
ction at the
'en (1956)
were
'hat

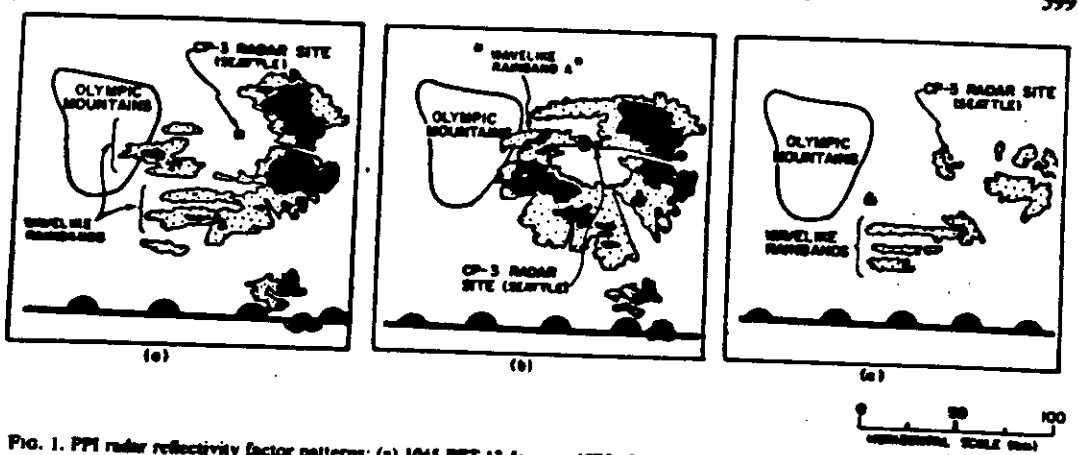

FIG. 1. PPI radar reflectivity factor patterns: (a) 1045 PST 13 January 1975, (b) 1115 PST on 13 January 1975 and (c) 1130 PST on 14 January 1975. Radar reflectivity factor values of 20–25 dBZ are indicated by the dotted areas and 25–30 dBZ by the black areas. [The circular shapes of the radar echoes associated with the lighter precipitation in (a) and (b) result from the radar beam, which was inclined 0.9° from the horizontal, encountering the lower values of radar reflectivity factor which were present at altitudes 1.2 km.] The approximate position of the warm-frontal surface at 1.5 km altitude is shown in each case.

lower level clouds. Simple trajectory calculations were made to further confirm the "seeding" of lower level clouds in this manner. To summarize the results of these calculations, we found that at 5 km altitude, 77% of the total mass of precipitation particles present was contained in partially rimed aggregates > 0.5 mm in diameter. The concentrations of these particles at this level were ~2 ℓ^{-1}. Based on particle fallspeed measurements made by Locatelli and Hobbs (1974), unrimed aggregates in

usually associated with generating cells ~4–8 km in diameter or with the precipitation trails emanating from them. This suggests that the generating cells were important sources of cloud and precipitation particles in the seeder zone. Based on *in situ* sampling, as well as radar measurements, we estimate that 20–40% of the mass of ice particles in the seeder zone were directly associated with generating cells, which occupied roughly 10–30% of the area observed in the seeder zone. A significant additional

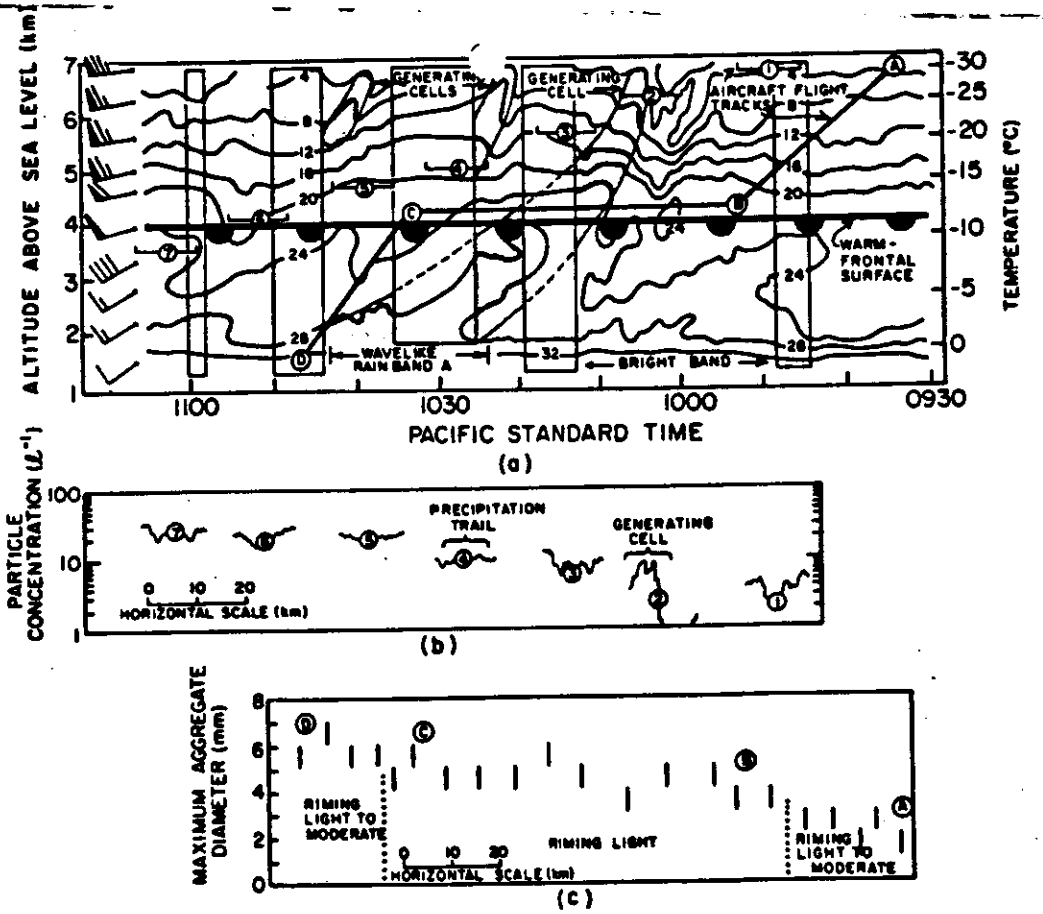

FIG. 2. Vertically pointing radar and aircraft measurements over Seattle on 13 January 1975. (a) Time-height section of the radar reflectivity factor (isopleths labeled in dBZ) with precipitation trails (shaded) and aircraft flight tracks (heavier lines labeled 1–7 and A–D). Rectangles enclose regions where vertically-pointing radar data were not collected. (b) Particle concentrations (70–1040 μm in maximum dimensions) measured along flight tracks 1–7 in (a). (c) Maximum size of ice particle aggregates and degree of ice particle riming along flight track ABCD in (a). The vertical profile of the wind is also shown in (a).

a feeder zone for precipitation growth both inside and outside the wavelike rainbands. The increase

growth of ice particles by deposition and aggregation was far more important than growth by riming. To quantify the picture which has been described

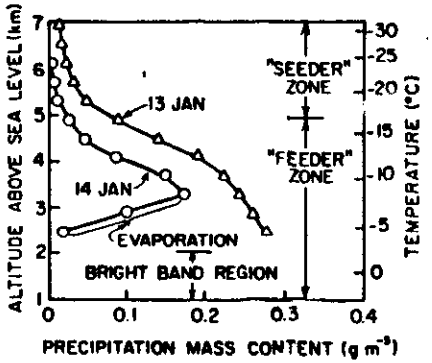

FIG. 4. Vertical profiles of precipitation mass content derived from radar reflectivity factor measurements on 3 and 14 January 1975.

Shown in Fig. 4 are vertical profiles of M, calculated from (1) using average values of Z measured above the radar. The curve for 13 January covers the time period shown in Fig. 3a. The values of M in Fig. 4 are averages and are based on measurements obtained both within and between precipitation trails. Values of M in the radar bright band region are not shown in Fig. 4 since (1) is not necessarily valid in this region. Increases of M with decreasing height are indicative of precipitation growth, while decreases of M with decreasing height (e.g., below 3.3 km for the 14 January curve in Fig. 4) are due to evaporation. It can be seen from Fig. 4 that the particle growth which took place in the seeder zone on both days resulted in average precipitation mass contents which were ~20% of the maximum mass contents in each profile. The remaining 80% of the precipitation mass was produced in the feeder zone. These figures demonstrate the importance of ice par-

a particle nucleated at upper levels and g
deposition at the observed relative humidi
have reached a diameter much larger tha
while falling into the lower parts of the clo
it seems likely that some form of ice mu
was responsible for the high concentratio
ice particles observed in the lower porti
clouds. Multiplication by the fragmentat
liding precipitation particles, which has
cussed by Hobbs and Farber (1972) and
(1978), could have been important, espec
region below the −16° level where der
moderately rimed aggregates were presen
nent increase in the concentrations of sm
can be seen in this region on 13 and
(Fig. 5). A second possible ice mu
mechanism is the ejection of ice splinters
droplets involved in riming in the temper
from −3 to −8°C (Hallett and Mossop,
servations of rimed particles (Fig. 2c) and
patches of liquid water in this temper
suggest that this mechanism may have
on 13 January. On 14 January, when p
centrations were generally lower, liquid
not observed in the necessary temper
for the Hallett-Mossop mechanism to o

d. Vertical air motions in and out of the

The widespread stratiform cloud and
cipitation growth which was observed
hours within the feeder zones suggests
spread stratiform updraft was present
sensitivity of direct measurements by
Doppler radar is generally not sufficien
measure such updrafts (usually a few t
meter per second), their magnitudes
inferred through indirect methods. One s

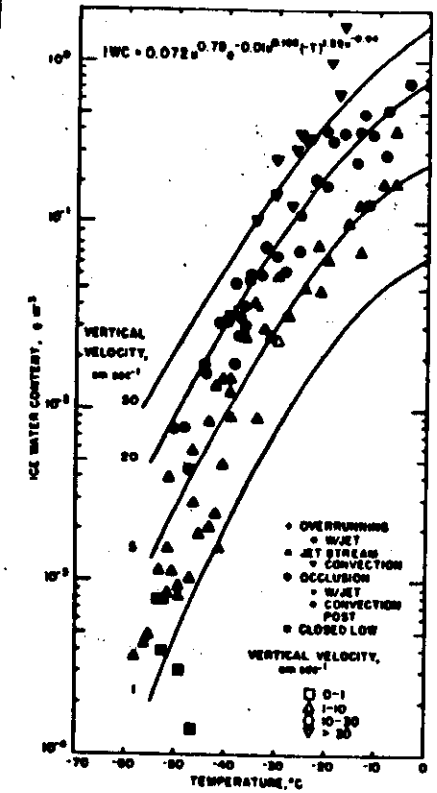

FIG. 5. Ice water content plotted against temperature, and parameterized in terms of the vertical air velocity: inside symbol, synoptic type; outside symbol, vertical velocity range. Best-fit equations to data are indicated.

$z > z_c$, when the dBZ or IWC and temperature values are plotted or if the z and temperature value is plotted and if $IWC_c > IWC$ or $dBZ_c > dBZ$.

Fig. 4a permits determination of the presence or absence of liquid water through utilization of a Doppler radar. Given measured dBZ and $\bar{v}$ values, the updraft velocity can be determined through utilization of the $\bar{v}-Z$ relationship appearing in Section 5g. By comparing the threshold vertical velocity with the value calculated from the $\bar{v}-Z$ relationship, it can be determined whether liquid water exists.

Fig. 4b permits determination of threshold vertical velocities necessary to produce liquid water in the synoptic types discussed in Section 3. Average ice water content values for warm frontal overrunning systems and warm frontal occlusions are plotted according to the average vertical velocity (Section 5a) and temperature in the figure. For overrunning systems, the average vertical velocities are below the threshold velocity from −30°C to warmer than −5°C. This indicates that liquid water will form in deep warm frontal overrunning systems only with strong vertical velocities or near the cloud top or leading edge where the ice water content is very low. For warm frontal occlusions typical of those observed in the present study, the vertical velocity is generally insufficient to produce liquid water except with quite vigorous updrafts. Liquid water would be expected to occur in a deep stratiform cloud with weak vertical velocities at temperatures between 0° and −5°C. The conclusions described above are in agreement with observations of liquid water discussed in Section 3 and plotted in Fig. 4b.

d. Ice water content and ice crystal habits

The ice water content was parameterized in terms of vertical velocity and temperature. Ice water content

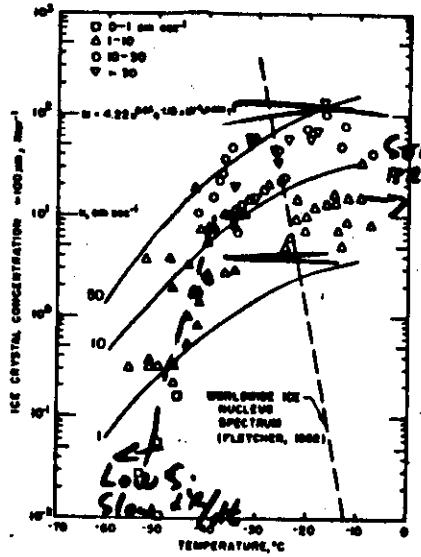

FIG. 6. Total ice crystal concentration (>100 μm) plotted against temperature and parameterized in terms of the air velocity. Best-fit equations to these data points are indicated. Worldwide ice nucleus spectrum is plotted.

introduced because the actual spectral shape at the warmer temperatures may not be the same as that assumed for the −5°C determination of $A'(T)$. The dependence of dBZ_c was found in a similar manner since $dBZ_c = G\bar{v}$.

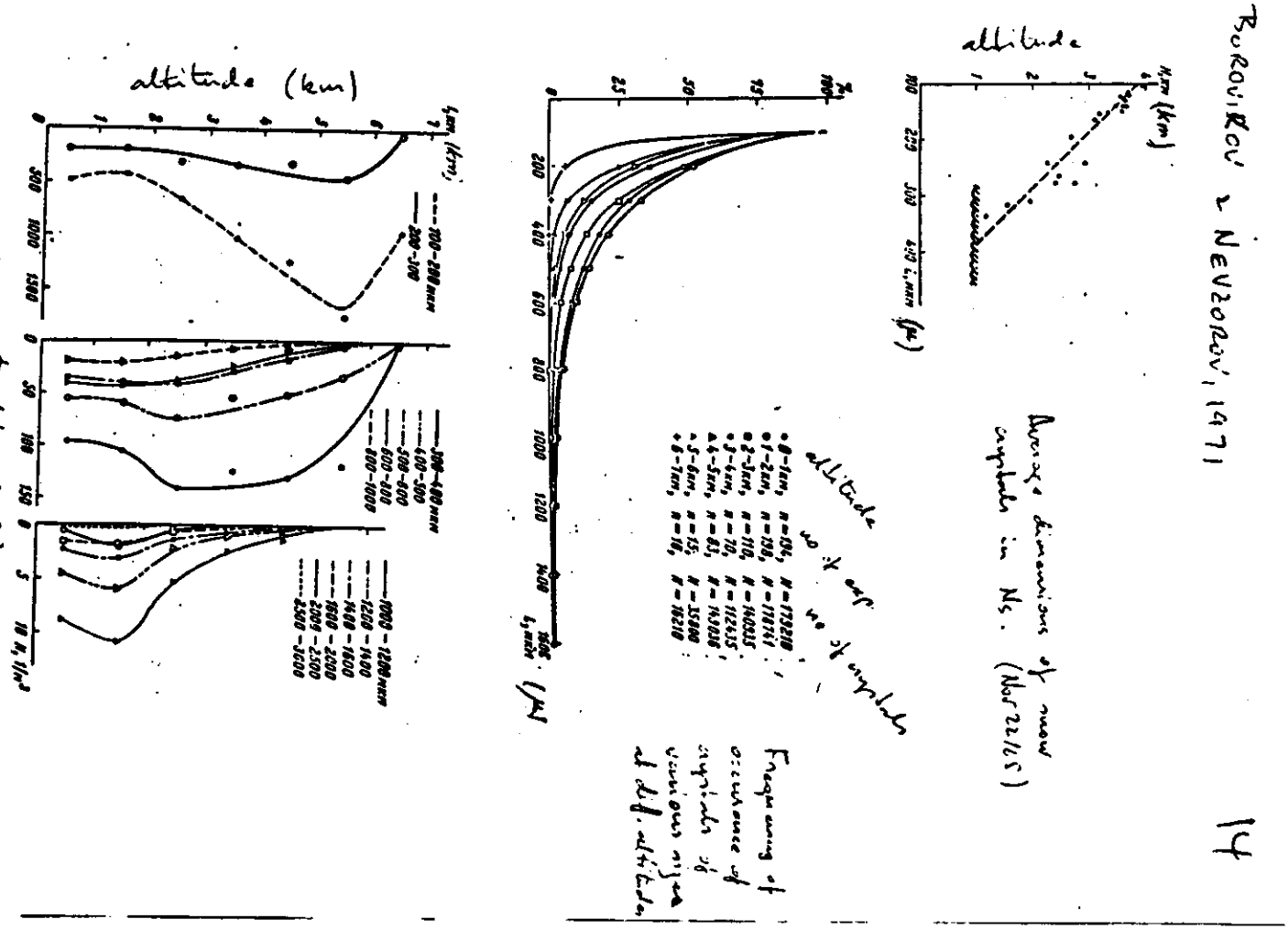

March 1980). One ASD was performed on each da, and these will be referred to as spirals 1, 2 and 3 respectively.

All three spirals took place in winter cyclonic storms. Spiral 1 was flown just ahead of an occluded front and spiral 2 was flown ~100 km east of a low-pressure center. Spiral 3 was flown in the warm sector of a cyclonic storm. The soundings obtained from the aircraft data indicated that the atmosphere was slightly more stable than moist adiabatic and was saturated in all cases. The height and temperature ranges for the three spirals are given in Table 1. No significant supercooled water was detected in any of the storms.

remains relatively constant through loop 12, after which there is a rapid decrease in both the slope and intercept during loops 13 and 14. The remainder of the loops show essentially no change. The vertical separation between successive loops is 200 m.

Because of the quasi-exponential behavior it is convenient to characterize the spectra by N_0 and λ which can be done via a least-squares fit. Fig. 5 shows data from the three spirals in $\log_{10}N_0$-$\log_{10}\lambda$ (hereafter N_0-λ space). The loop numbers are indicated next to the data points which are connected sequentially by a line. Environmental temperatures are indicated for places where significant changes occur.

Lo, Passarelli, 1982

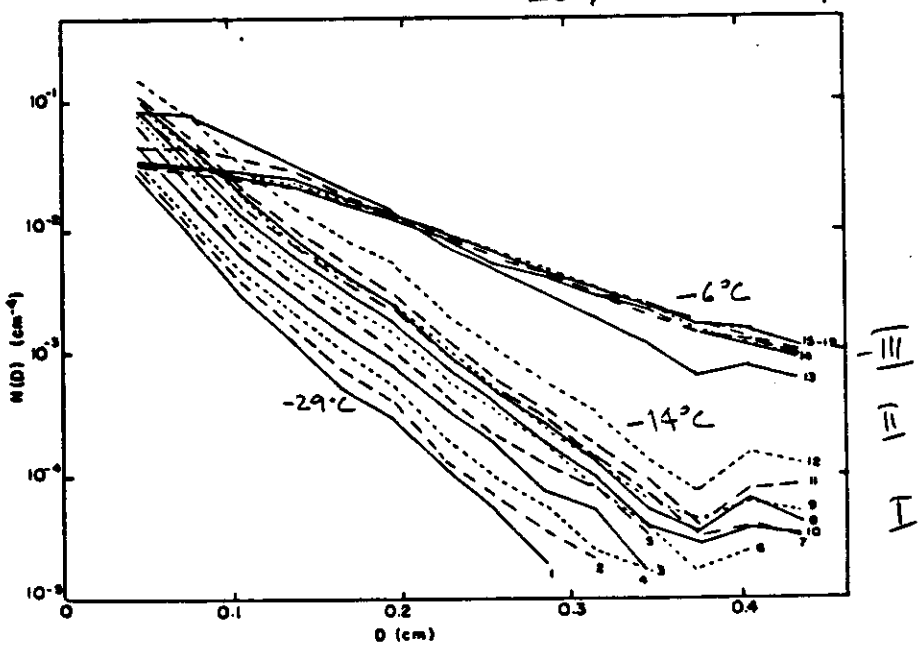

FIG. 4. Snow size spectra for spiral 1 (25 February, 1980) averaged over the various loops. Numbers on the right indicate loop numbers.

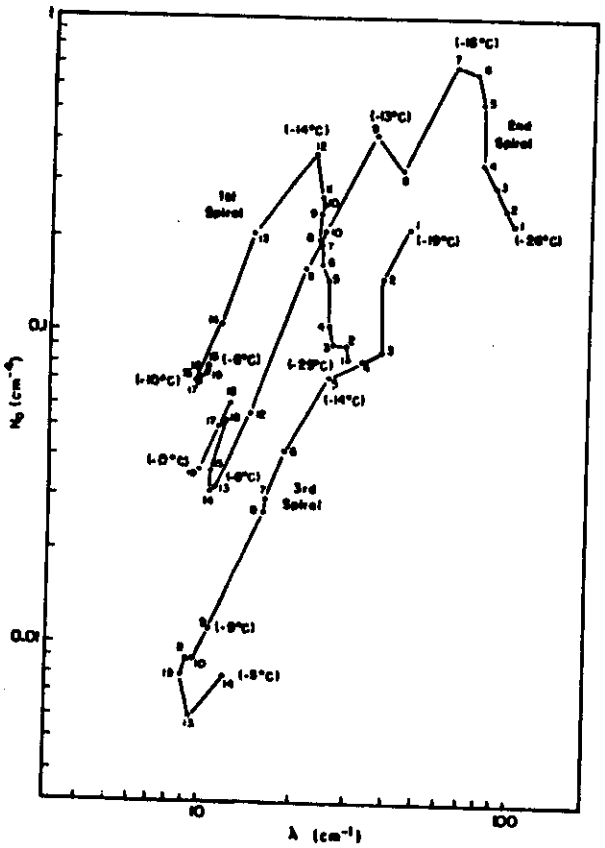

FIG. 5. N_0–λ trajectories for the three spirals. See text for details.

This type of spectral display is convenient because raight line in N_0–λ space corresponds to a con- it moment of an exponential distribution, since jth moment of a spectrum is

$$M_j = \int_0^\infty D^j N_0 e^{-\lambda D} dD = \frac{N_0 \Gamma(j+1)}{\lambda^{j+1}}. \quad (9)$$

ce in logarithmic N_0–λ space, the moment M_j onstant along any straight line having slope (j).

he behavior of the spectra in Fig. 4 can be dis- ed in terms of the trajectory of the spectral evo- n in N_0–λ space in Fig. 5. The first spiral is

acterized by an increase in N_0 accompanied by relatively little change in λ. Stage 2 is characterized by a rapid decrease in both N_0 and λ. Stage 3 is marked by an apparent cessation of spectral evolution. The third spiral only reveals stages 2 and 3.

The N_0–λ trajectories for the second stage of growth are roughly parallel for all three spirals, having slopes ranging from 1.80 to 1.95. This suggests that during this phase of spectral evolution, the sum of the diameters of snow particles is a conservative property of the distribution. These three cases also suggest that the distribution slope, λ, has a minimum value of ~10 cm^{-1} which characterizes the third stage of evolution.

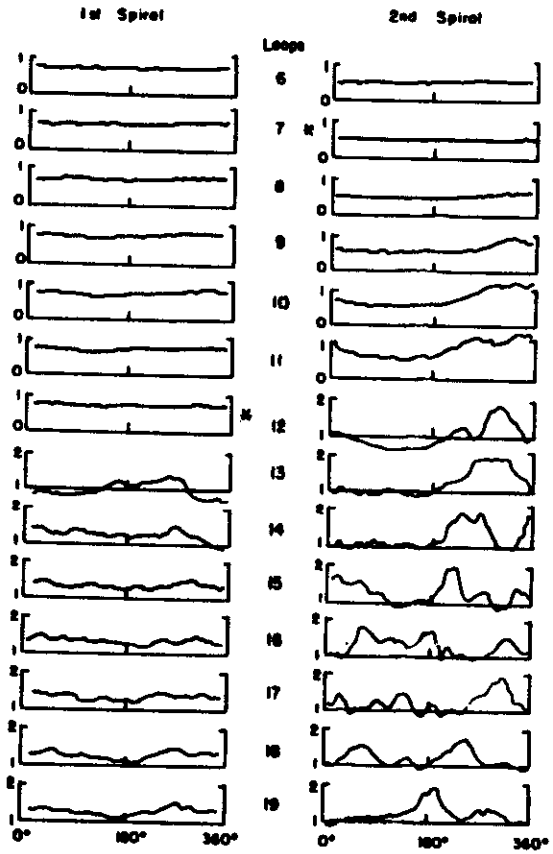

FIG. 6. Average particle diameter as a function of magnetic heading for spirals 1 and 2. Diameters in mm.

1st and 2nd spirals. Each loop is represented by a separate graph and the loops are stacked vertically in accordance with their height. The approximate diameter of each loop is 6 km. The loop in which the spectra transformed from first to second stage growth (the peak in the N_0–λ trajectory) is indicated by a star in each case. Before the transition, the mean diameter is essentially uniform within each loop and gradually increases with depth. (Not all upper-level loops are shown). However, after the transition, horizontal inhomogeneities develop very rapidly. Note that the features are correlated from one loop to the next.

In order to examine the point-to-point behavior of the spectra, we arbitrarily divide each loop into

is different for each quadrant in order to s the four quadrants. Note that the four N_0–λ tories all show the same general features. H the west–north quadrant starts rapid stage 2 earlier than the other quadrants (e.g., examir 9 and 10 in Fig. 6).

Fig. 7 illustrates that even if we examine p of a loop the spectral evolution is coherent. consistent with the previous discussions. A rapid development of horizontal gradients o diameter are apparently related to the fact th tra in different regions undergo the transitic stage 1 to stage 2 at different heights.

4. Physical interpretation of ASD condi-

Carbone & Bohne 1975

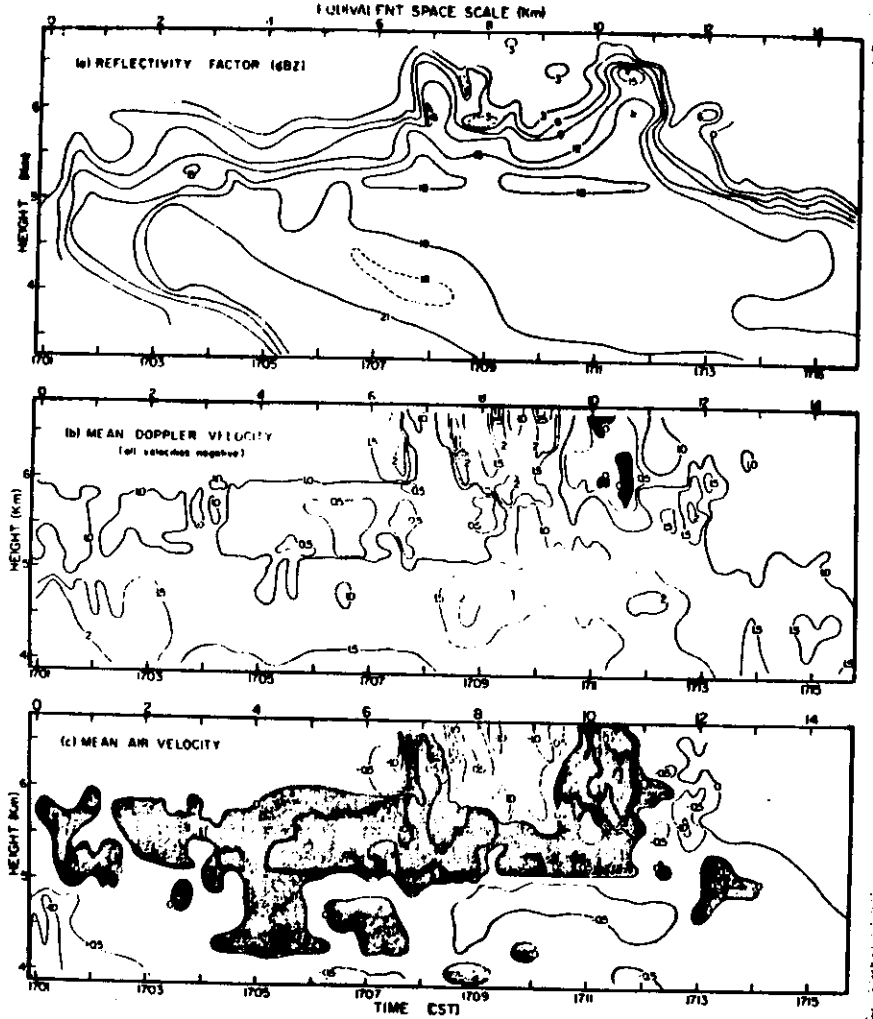

FIG. 1. Digitized time-height sections of (a) reflectivity factor, (b) mean Doppler velocity and (c) estimated mean air velocity. See text for explanation.

A clearer picture of vertical air motion may be obtained by the assumption of a relationship between mean, reflectivity-weighted, particle velocity $\bar{v}_p$ and the reflectivity factor Z. The correct choice of a $\bar{v}_p$-Z relationship is dependent upon the particle size distribution and the terminal velocity vs size dependence. A family of such relationships exists in the literature, some of which are more appropriately applied to single crystal snow and others to rimed crystals or aggregates. Several relationships of the form $\bar{v}_p = cZ^k$ were tested

The terminal velocities for a precipitating particle of diameter D_R, D_S or D_G are

TABLE 1. Key to Fig. 1

Symbol	Meaning
P_{IMLT}	Melting of cloud ice to form cloud water. $T \geq T_0$.
P_{IDW}	Depositional growth of cloud ice at expense of cloud water.
P_{IHOM}	Homogeneous freezing of cloud water to form cloud ice.
P_{IACR}	Accretion of rain by cloud ice: produces snow or graupel depending on the amount of rain.
P_{RACI}	Accretion of cloud ice by rain: produces snow or graupel depending on the amount of rain.
P_{RAUT}	Autoconversion of cloud water to form rain.
P_{RACW}	Accretion of cloud water by rain.
P_{REVP}	Evaporation of rain.
P_{RACS}	Accretion of snow by rain: produces graupel if rain or snow exceeds threshold and $T < T_0$.
P_{SACW}	Accretion of cloud water by snow; produces snow if $T < T_0$ or rain if $T \geq T_0$. Also enhances snow melting for $T \geq T_0$.
P_{SACR}	Accretion of rain by snow. For $T < T_0$, produces graupel if rain or snow exceeds threshold; if not, produces snow. For $T \geq T_0$, the accreted water enhances snow melting.
P_{SACI}	Accretion of cloud ice by snow.
P_{SAUT}	Autoconversion (aggregation) of cloud ice to form snow.
P_{SFW}	Bergeron process (deposition and riming)—transfer of cloud water to form snow.
P_{SFI}	Transfer rate of cloud ice to snow through growth of Bergeron process embryos.
P_{SDEP}	Depositional growth of snow.
P_{SSUB}	Sublimation of snow.
P_{SMLT}	Melting of snow to form rain, $T \geq T_0$.
P_{GAUT}	Autoconversion (aggregation) of snow to form graupel.
P_{GFR}	Probabilistic freezing of rain to form graupel.
P_{GACW}	Accretion of cloud water by graupel.
P_{GACI}	Accretion of cloud ice by graupel.
P_{GACR}	Accretion of rain by graupel.
P_{GACS}	Accretion of snow by graupel.
P_{GSUB}	Sublimation of graupel.
P_{GMLT}	Melting of graupel to form rain, $T \geq T_0$. (In this regime, P_{GACW} is assumed to be shed as rain.)
P_{GWET}	Wet growth of graupel; may involve P_{GACS} and P_{GACI} and must include P_{GACW} or P_{GACR}, or both. The amount of P_{GACW} which is not able to freeze is shed to rain.

Lin, Farley & Orville, 1983

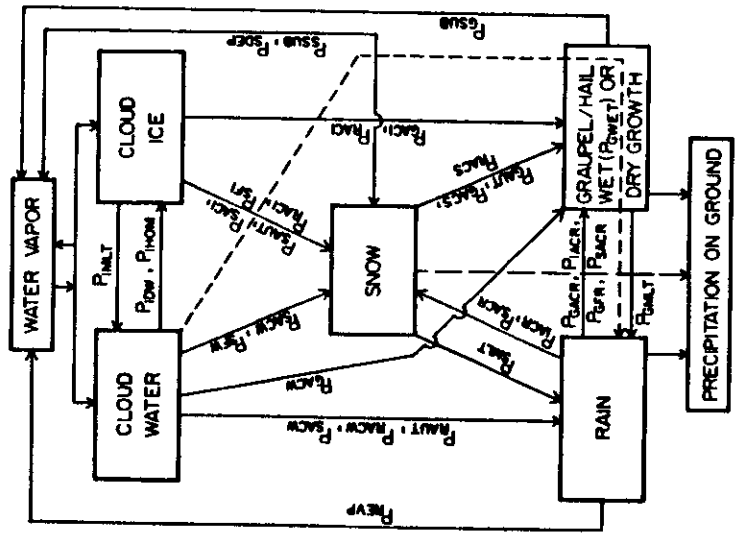

FIG. 1. Cloud physics processes simulated in the model with the snow field included. See Table 1 for an explanation of the symbols.

1) PARAMETERIZATION

19

$$\lambda_R = \left(\frac{\pi \rho_W n_{0R}}{\rho l_R}\right)^{0.25}, \quad (4)$$

$$\lambda_S = \left(\frac{\pi \rho_S n_{0S}}{\rho l_S}\right)^{0.25}, \quad (5)$$

$$\lambda_G = \left(\frac{\pi \rho_G n_{0G}}{\rho l_G}\right)^{0.25}, \quad (6)$$

where l_W, l_S and l_G are densities of water, snow and hail, respectively. The density of snow is assumed to be 0.1 g cm^{-3} in this study. The symbols l_R, l_S and l_G are mixing ratios of rain, snow and hail, respectively.

The terminal velocities for a precipitating particle of diameter D_R, D_S or D_G are

TABLE 1. Key to Fig. 1

Symbol	Meaning
P_{IMLT}	Melting of cloud ice to form cloud water. $T \geq T_0$.
P_{IDW}	Depositional growth of cloud ice at expense of cloud water.
P_{IHOM}	Homogeneous freezing of cloud water to form cloud ice.
P_{IACR}	Accretion of rain by cloud ice; produces snow or graupel depending on the amount of rain.
P_{RACI}	Accretion of cloud ice by rain; produces snow or graupel depending on the amount of rain.
P_{RAUT}	Autoconversion of cloud water to form rain.
P_{RACW}	Accretion of cloud water by rain.
P_{REVP}	Evaporation of rain.
P_{RACS}	Accretion of snow by rain; produces graupel if rain or snow exceeds threshold and $T < T_0$.
P_{SACW}	Accretion of cloud water by snow; produces snow if $T < T_0$ or rain if $T \geq T_0$. Also enhances snow melting for $T \geq T_0$.

Stewart et al 1984
J.A.S. p. 3227

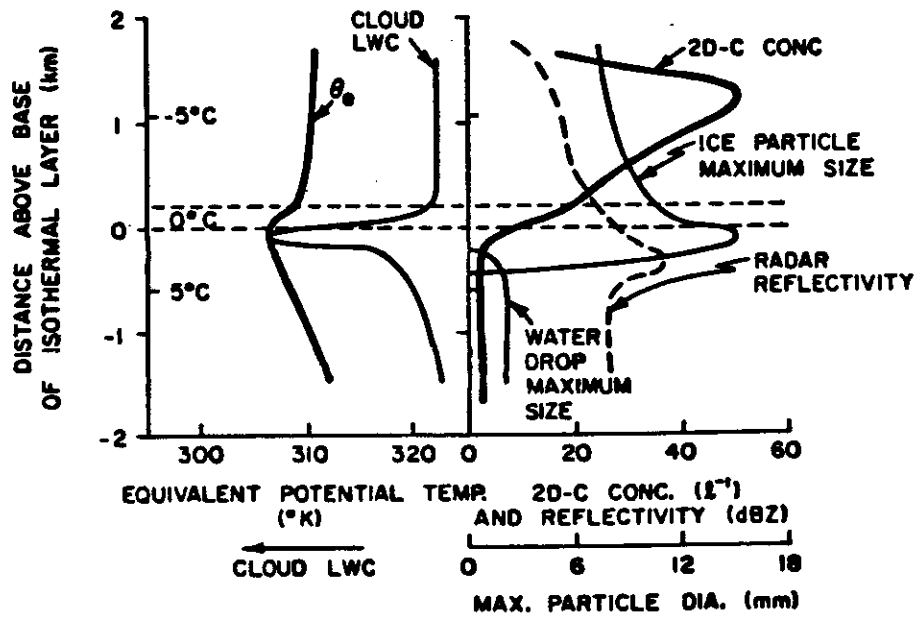

FIG. 13. Schematic profile illustrating significant trends of various microphysical and state parameters through a typical melting layer as deduced by synthesizing the observations of all the case studies.

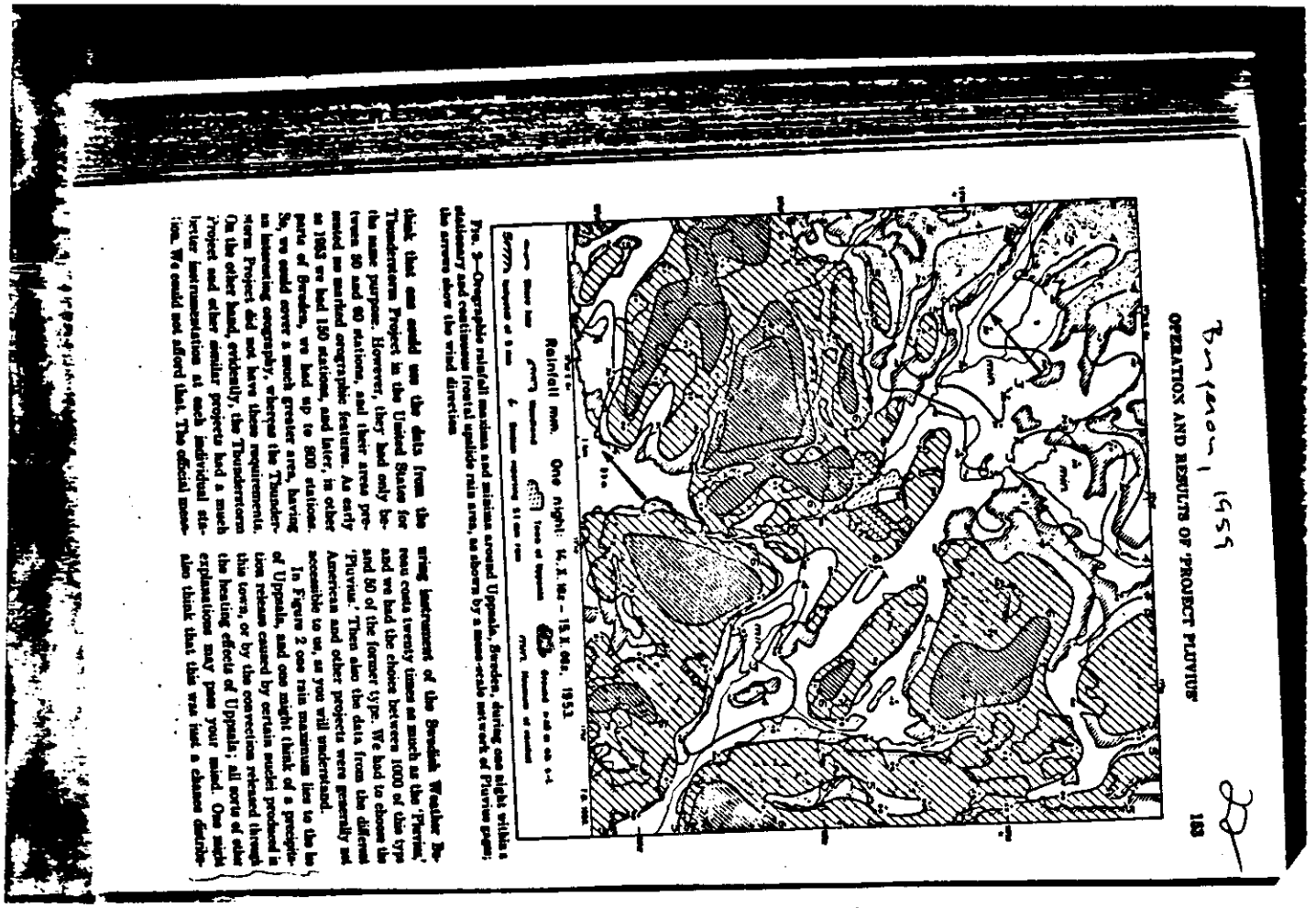

OPERATION AND RESULTS OF 'PROJECT PLUVIUS'

183

Fig. 3—Orographic rainfall maxima and minima around Uppsala, Sweden, during one night within a stationary and continuous frontal rainfall area, as shown by a meso-scale network of Pluvius gages; the arrows show the wind direction.

think that one could use the data from the Thunderstorm Project in the United States for the same purpose. However, they had only between 80 and 90 stations, and their areas presented no marked orographic features. As early as 1933 we had 150 stations, and later, in other parts of Sweden, we had up to 500 stations. So, we could cover a much greater area, having a interesting orography, whereas the Thunderstorm Project did not have these requirements. On the other hand, evidently, the Thunderstorm Project and other similar projects had a much better instrumentation at each individual station. We could not afford that. The official measuring instrument of the Swedish Weather Bureau costs twenty times as much as the 'Pluvia,' and we had the choice between 1000 of this type and 80 of the former type. We had to choose the latter. Then also the data from the different American and other projects were generally not accessible to us, as you will understand.

In Figure 2 one rain maximum line to the lee of Uppsala, and one might think of a precipitation release caused by certain model produced in this town, or by the convection released through the heating effects of Uppsala; all sorts of other explanations may pass your mind. One might also think that this was just a chance distribution. We do not think that this is the case, but we

on the windward slopes of the hills and ...

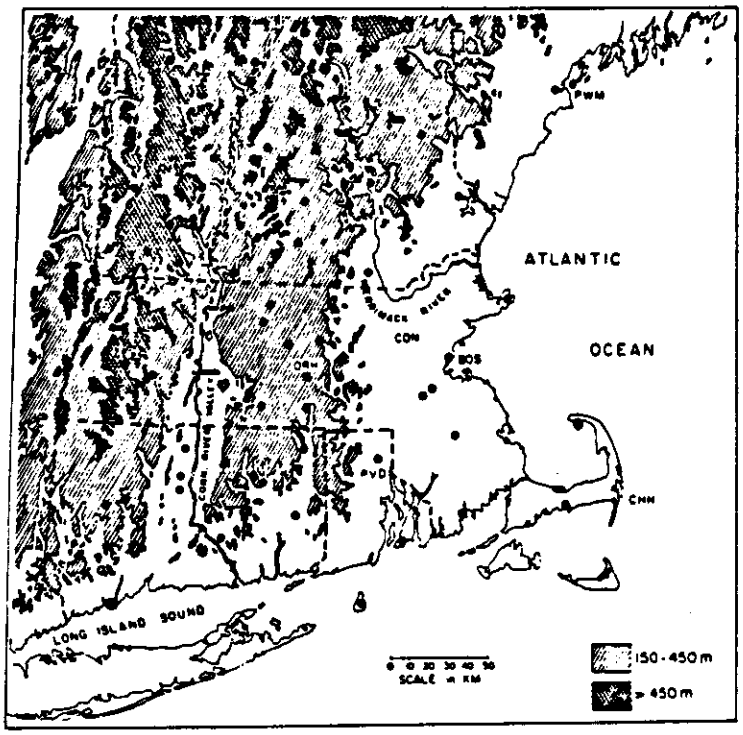

FIG. 1. Terrain of southern New England and the locations of the raingauges.

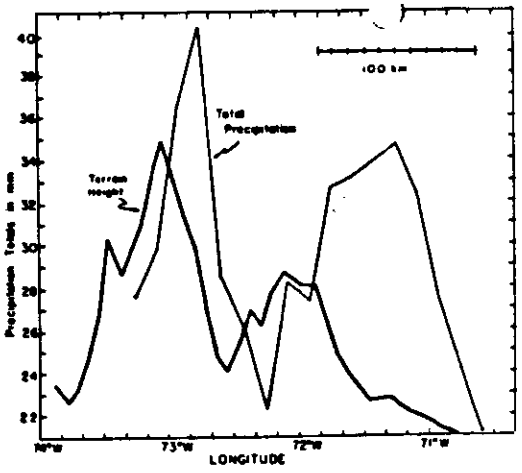

FIG. 5. Average precipitation total as a function of longitude for Massachusetts. The terrain elevation from Fig. 2 is ... for reference.

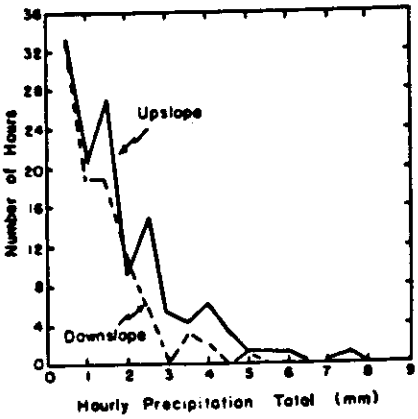

FIG. 8. Precipitation rate spectra for two proximal upslope and downslope stations for eight storm events. See text for details.

ven thin (~500 m) orographic clouds can account or the observed upslope anomalies. The analyses also uggest that frictionally-induced convergence may act

ture of these two resolutions for the s studied.

Fig. 2 is an east–west cross-sectior

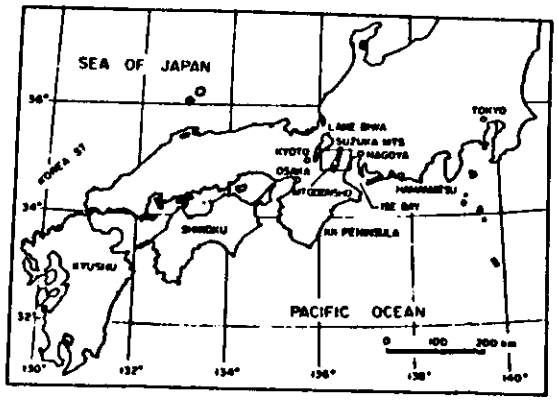

(a)

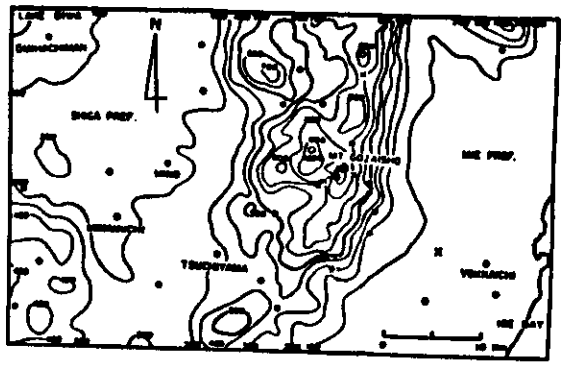

(b)

Fig. 1 (a) Map of Central and Western Japan. (b) Topographic map around the Suzuka Observation points of rainfall: ● by local mountains. Contour lines: 100 m intervals. Meteorological Observatories and Regional Construction Bureaus; ⊗ and × our special observation points set up until 1968 and 1970 respectively.

along the south-east bounda
Lake Biwa and are centered
1,210 m in height (Fig. 1(a)
topography around the Suzu
aged with a grid of 1 km is
tains extend nearly north
average height of about 800
points are also shown in Fig.
is believed to be one of the m
laid out, with a mean densit
60 km².

This area is the rainiest in
cording to our observations,
cipitations (9h–9h JST) of 100
300 mm occurred about five
year, respectively, and one c
of more than 300 mm occur
on the average, during a pe
(1967–1976). The maximum
recorded here was 626 mm o
(Gocho, 1973).

Two examples of typical oro
fall without association of a r
scope, as shown later, were
curred on 29 July and 25 Sept
distributions of daily precipitat
are shown in Fig. 2 (a) an
(Gocho and Nakajima, 1972).
maximum daily precipitation
mm was observed at a point
ridge, while the heavy rainfall
ridge. Typhoon 6804 travel
westwardly in the vicinity of
shu on 29 July, and typhoon
stagnant west of Kyushu on 2

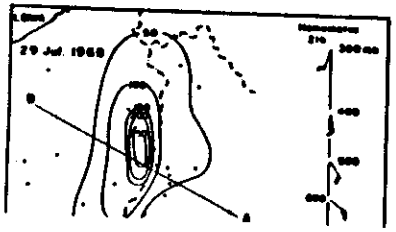

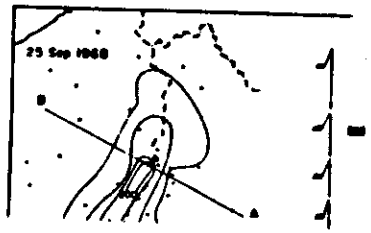

(b)

Fig. 1 (a) Map of Central and Western Japan. (b) Topographic map around the Suzuka Observation points of rainfall: ● by local mountains. Contour lines: 100 m intervals. Meteorological Observatories and Regional Construction Bureaus; ⊗ and × our special observation points set up until 1968 and 1970 respectively.

(Gocho and Nakajima, 1972). In ei case a maximum daily precipitation of more than 200 mm was observed at a point just west of the ridge, while the heavy rainfall area lay along the ridge. Typhoon 6804 travelled slowly northwestwardly in the vicinity of Shikoku and Kyushu on 29 July, and typhoon 6816 was almost stagnant west of Kyushu on 25 September. The

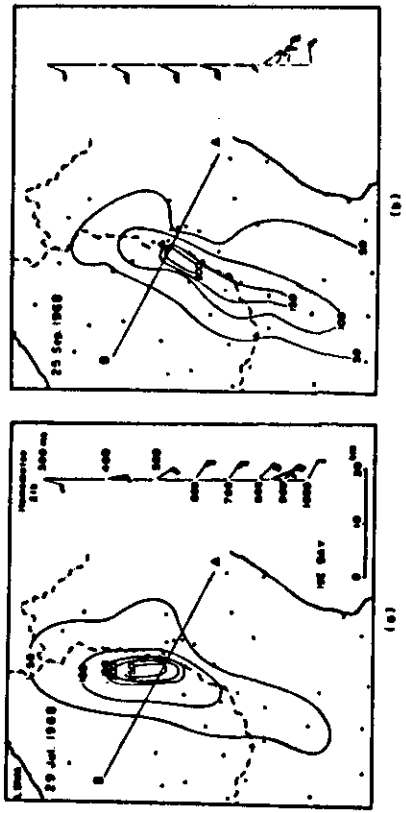

Fig. 2 Distributions of daily precipitation in mm (9h–9h JST) around the Suzuka mountains and the vertical distributions of wind (a long barb 10 knots) for 21h at Hamamatsu, on 29 July (a) and 25 September (b) in 1968.

of
nilar
pitation
y under-
increase
ng is not
d Bader
of pre-
h a two-
. Their
r. It is
rove the
ountains
In this
rainfall
f drops
s taken

e heavy

graphic
ins will
merical
an the
m sea-
ch lay

he sea and by forced orographic ascent over hills. The release of this PI and the ng localized outbreaks of convection led to prolonged rainfall at rates between 2 and hr^{-1} over the Welsh hills and extensive light rain over central England.

model illustrating the dependence of the rainfall distribution in the warm sector on ease of PI has been synthesized from the results in Sections 4 and 5. The model is in Fig. 12 and an explanation of the symbols used in the model is given in the Key.

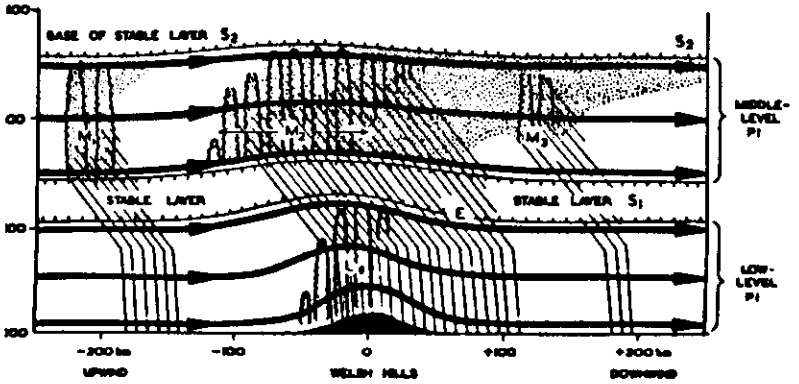

12. Model showing dependence of warm sector rainfall on potential instability and orography. See Key for explanation of symbols.

Mean streamlines within the strong west-south-west flow crossing the Welsh hills, drawn to be consistent with the observed pattern of precipitation development; although the precise form of the streamlines is arbitrary, notice that the middle-level air begins to ascend far upwind of the hills.

Layer with rather high static stability separating the potentially unstable air at low levels from potentially unstable air at middle levels.

Base of the region of high static stability that extends throughout the upper troposphere.

Small scale convection occurring where the low-level or middle-level potential instability (PI) is realized by general ascent.

Ice crystal (anvil) 'cloud' resulting from the middle-level convection and perhaps also, above 500 mb, from stable ascent over the hills.

Precipitation trajectories relative to the ground, strongly inclined because of the high winds; the change in slope occurs at the melting level at about 840 mb.

I_1 Middle-level convection within isolated MPAs due to areas of mesoscale ascent that occur in the warm sector even over the sea.

I_2 Abundant middle-level convection triggered by orographic uplift over the hills, occurring as fresh outbreaks within and between existing MPAs.

I_3 Decaying middle-level convection mainly associated with MPAs previously in existence far upwind of the hills (i.e. M_1).

Rapid low-level growth of precipitation falling from aloft, producing a large increment in rainfall rate tied closely to the hills.

E Evaporation in the lee of the hills, decreasing the amount of precipitation from middle-levels that reaches the ground over central England; however, because of the enhanced generation of precipitation over the hills (M_2) widespread rain continues to fall up to 100 km downwind of the hills.

26

Browning et al., 1974, QJRMS p 309

E = 12%

Figure 1. The variation of the maximum precipitation enhancement (ΔR mm h^{-1}) as a function of windspeed and shear model formulation for ... h_1 = 600 m, Z_0 = 1200 m. The variation is denoted in ...

Carruthers - Choularton 1983

27

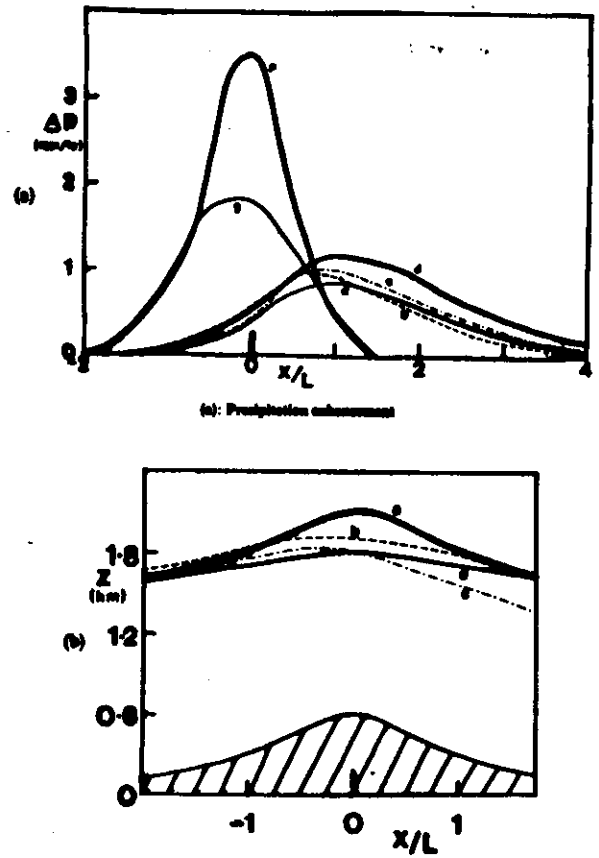

Figure 2. Precipitation enhancement and cloud top streamline height as a function of distance over the ... hill. P_0 = 1·5 mm h^{-1}. The curves corresponding to the 3D model are not shown because of the difference in the profile.

cloud near the summit reach the ground downwind of the topography where the feeder cloud has evaporated.

Over the short hill when wind drift is included the efficiency of washout E_w, as defined in (BR), is very small: $E_w \approx 5\%$ for $P_0 = 0{\cdot}5$ mm h^{-1} rising to $\approx 12\%$ for $P_0 = 2{\cdot}5$ mm h^{-1}. These values are approximately two thirds of the values obtained when wind drift is not included and so the total enhancement is also decreased. This decrease due to

models (b, c, d) are small and their average is smaller than the predictions of (SR). In particular the inclusion/exclusion of condensation effects in the airflow model has only a small effect on the enhancement and indeed the stratified models predict enhancements similar to the two-dimensional potential flow model. The three-dimensional model results in somewhat smaller enhancements due to some flow round rather than over the hill; this small decrease is, however, hardly observable.

(d) Orographic enhancement over 'long' hills of a given height. Figures 3 and 4 present a similar set of graphs for a much longer less steep hill ($L = 20$ km, $h = 600$ m). In this case $L_v \gg L_d$ (Eqs. 2 and 3) and wind drift does not change the rainfall distribution, but it is translated downwind a distance L_d. The (SR) model (a) is seen to agree very well with the potential flow models (d and e) and three-dimensional effects are negligible.

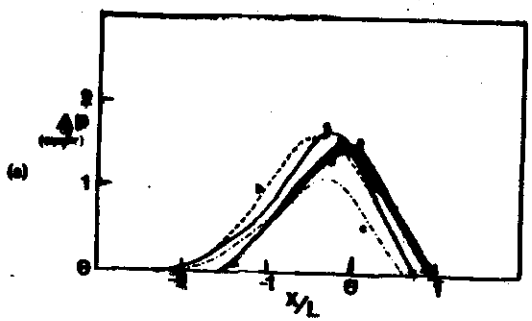

(a): Precipitation enhancement

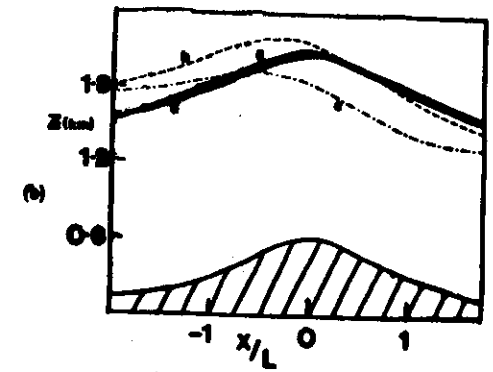

(b): Cloud top streamline height

Figure 4. Precipitation enhancement and cloud top streamline height as a function of distance over the long hill. $P_0 = 1{\cdot}0$ mm h^{-1}.

COTTON 29

of 10 l^{-1} and varied little with altitude. The experiment was therefore repeated by specifying the concentration of activated ice crystals to be 10 l^{-1}, independent of cloud temperature. The results of this experiment are described below.

Figure 10 illustrates a cross section through the simulated cloud after 7200 s of simulated time. The crystal field exhibited a tendency to build windward from the first hour until the second hour. As in the observations, the peak liquid water contents were immediately over the windward side of the barrier. The magnitude of the peak varied somewhat in time from 0.36 g kg^{-1} (0.32 g m^{-3}) at 5400 s, to 0.40 g kg^{-1} (0.36 g m^{-3}) at 7200 s, in quite good agreement with observations.

Windward to the barrier, transient secondary zones of higher liquid water content and ice crystal mixing ratio are also evident in the simulation. The magnitude of peak liquid water content in the zones just windward of the slope, range from 0.06 to 0.09 g kg^{-1} (0.08 g m^{-3}) comparable to the magnitudes reported by Rauber. The total water maxima windward of −16.5 km shown in Figure 7 are composed almost totally of ice crystals. The absence of precipitating ice other than ice crystals in these « generating

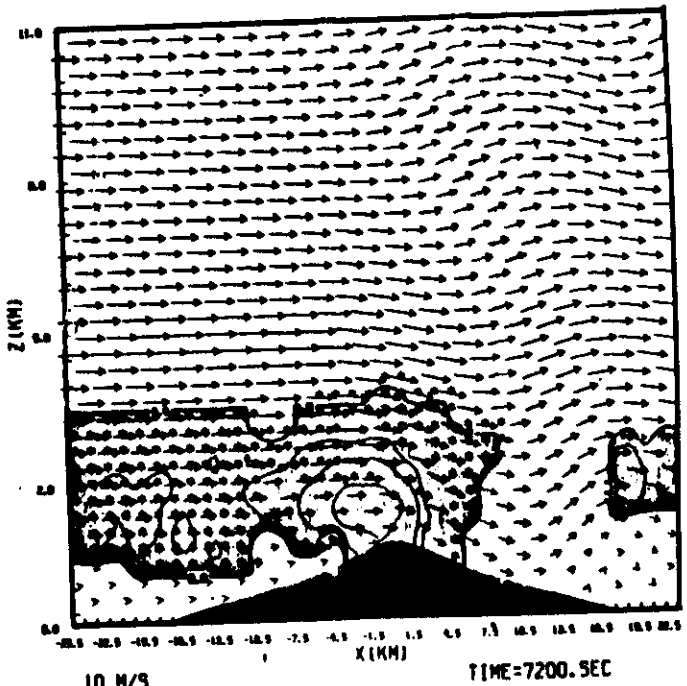

FIG. 10. — Z-X cross section through a simulated orographic cloud after 7200 s of simulated time. Shaded region represents water saturated regions. The ° represents regions having ice crystal mixing ratios greater than 0.01 g kg^{-1}. Contour intervals are for 0.1 g kg^{-1} of total condensate. Wind speeds are proportional to vector length shown on figure.

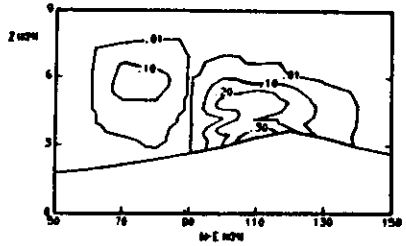

Figure 27. Mixing ratio of total ice (gm kgm^{-1}) along the wind at 3750 seconds into the integration.

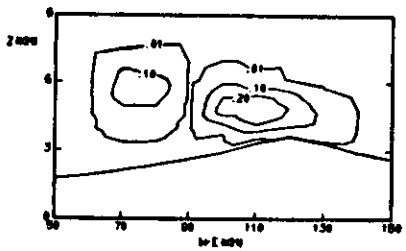

Figure 28. Mixing ratio of unrimed crystals (gm kgm^{-1}) along the wind at 3750 seconds into the integration.

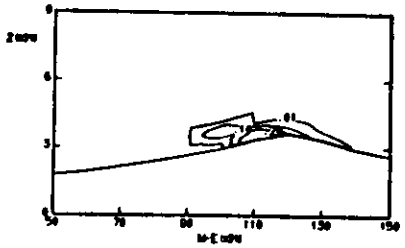

Figure 29. Mixing ratio of partially rimed crystals (gm kgm^{-1}) along the wind at 3750 seconds into the integration.

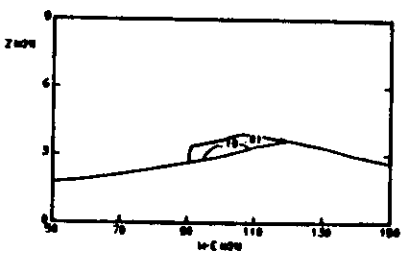

Figure 30. Mixing ratio of graupel (gm kgm^{-1}) along the wind at 3750 seconds into the integration.

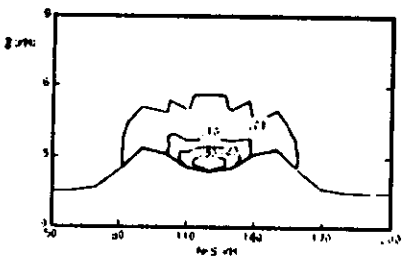

Figure 31. Mixing ratio of cloud water (gm kgm^{-1}) normal to the wind at 3750 seconds into the integration.

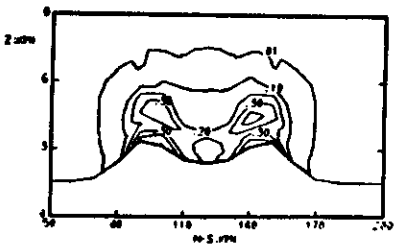

Figure 32. Mixing ratio of total ice (gm kgm^{-1}) normal to the wind at 3750 seconds into the integration. Dotted area denotes $q_i > 0.40$ gm kgm^{-1}.

Hanuity, 1985 35.
T.A.S. (to appear)

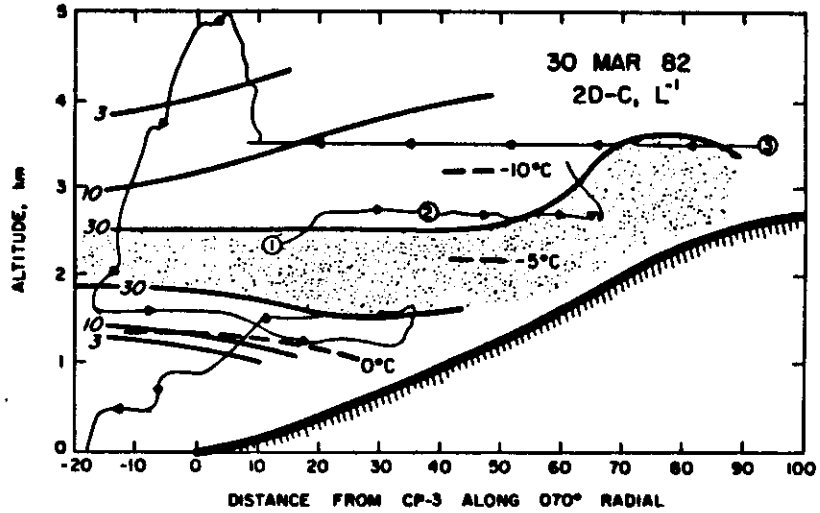

Fig. 3a Vertical cross-sections of King Air data on 30 Mar 1982 along the 070° radial from the CP-3 radar. The crest line is near 100 km and the CP-3 radar was near the upwind edge of the barrier. The analyzed fields are: a) 2D-C concentration of hydrometeors. A few key isotherms are indicated. The flight track is shown with arrows at 5-min intervals.

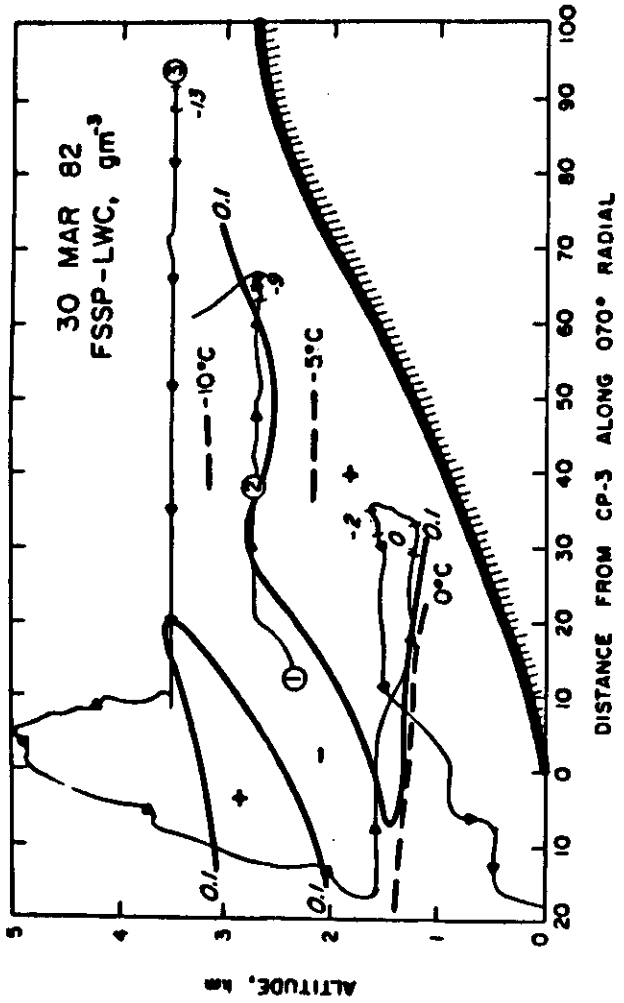

Fig. 3b. Integrated cloud water content from FSSP spectra. The flight intervals and mean temperatures for the cloud droplet spectra shown in Fig. 4 are indicated.

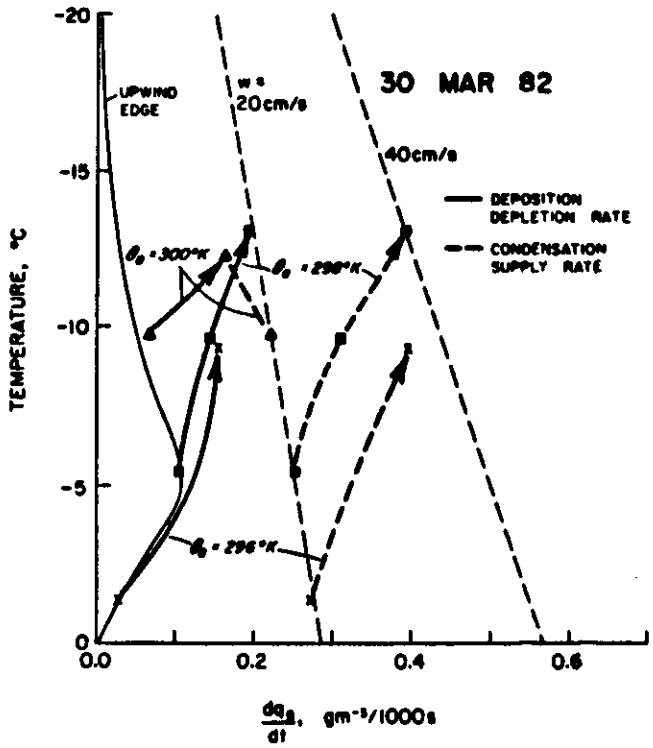

Fig. 7. Profiles of condensation supply rates and deposition depletion rates for 30 Mar 1982. See text for details.